Diagnosising the sensitivity of grounding line flux to changes in sub-ice shelf melting

Tong Zhang, Stephen Price, Matthew Hoffman, Xylar Asay-Davis

Fluid Dynamics and Solid Mechanics Group, Los Alamos National Laboratory, New Mexico, United States, 87545

Correspondence: Tong Zhang <tzhang@lanl.gov>

ABSTRACT. Motivated by previous work using ice flow models to quantify ice shelf buttressing and its impacts on the flux of ice across the grounding line (e.g., Fürst and others, 2016; Reese and others, 2018), we seek an improved physical understanding for how ice dynamics link small ice thickness perturbations, via changes in sub-ice shelf melting, to changes in ice shelf buttressing and ice flux across the grounding line. More specifically, we seek to define one or more "metrics" that are 1) readily calculated from standard ice sheet model outputs and 2) informative for diagnosing the sensitivity of grounding line flux to changes in ice thickness at specific locations on an ice shelf. By studying the ice dynamics for both idealized (MISMIP+) and realistic (Larsen C) ice shelves, we find that the first principle stress is the best overall metric for linking local changes in ice shelf thickness and dynamics with changes in the integrated grounding line flux. Unfortunately, this metric only shows a robust relationship with the integrated grounding line flux for regions near the center of an ice shelf; for points too near the grounding line or the calving front, no clear relationship exists between any of the readily calculable metrics explored here and changes in grounding line flux. This motivates our exploration of an adjoint-based method for defining grounding line flux sensitivity to local changes in ice shelf geometry. Using the same idealized

and realistic test cases, we demonstrate that this method is equivalent to the sensitivity analysis of (Reese and others, 2018) but requires only a single model adjoint solve. We conclude that the adjoint-based method can provide a means of analyzing grounding line flux sensitivity to changes in sub-ice shelf melting at model run time.

INTRODUCTION

Marine ice sheets like West Antarctica (and to a lesser extent, portions of East Antarctica) are grounded below sea level and their bedrock would remain so even after full isostatic rebound (Barletta and others, 2018). This and the fact that ice sheets generally thicken inland lead to a geometric configuration that is unstable; a small increase in flux at the grounding line thins the ice there, leading to floatation, a retreat of the grounding line into deeper water, further increases in flux (due to thicker ice), and further thinning and grounding line retreat. This theoretical "marine ice sheet instability" mechanism (Mercer, 1978; Schoof, 2007) is supported by idealized (Schoof, 2012; Asay-Davis and others, 2016) and realistic ice sheet modeling (Royston and Gudmundsson, 2016) experiments and some studies (Joughin and others, 2014; Rignot and others, 2014) argue that such an instability is currently under way along outlet glaciers of Antarctica's Amundsen Sea Embayment (ASE). The relevant perturbation for grounding line retreat in the ASE is thought to be intrusions of relatively warm, intermediate depth ocean waters onto the continental shelves, which have reduced the thickness and extent of marginal ice shelves via increased submarine melting (e.g., **?**). These reductions are critical because fringing ice shelves restrict the flux of ice across their grounding lines farther upstream – the so-called "buttressing" affect of ice shelves (Gudmundsson and others, 2012; Gudmundsson, 2013; De Rydt and others, 2015) – which makes them a critical control on ice flux from Antarctica to the ocean.

On ice shelves, gradients in hydrostatic pressure are balanced by the primarily extensional flow of ice towards the calving front (Mutter, 1983; Morland, 1987; Schoof, 2007) and, in theory, a one dimensional (x-z) ice shelf provides no buttressing (Schoof, 2007; Gudmundsson, 2013)[1]. For realistic, three-dimensional ice shelves however, buttressing results from three main sources: 1) compressive ice flow 2) lateral shear, and 3) "hoop" stress (Pegler and Worster, 2012). Both compressive and lateral shear stresses can supply backward resistance to extentional ice shelf flow, and the "hoop" stress is a transverse stress arising from azimuthal

[1] The ice shelf is also assumed to be monotonically decreasing in thickness from the grounding line to the calving front.

extension in regions of diverging flow (Wearing, 2016). Due to the complex geometries, kinematics, and dynamics of real ice shelves, an understanding of the specific processes and locations that control ice shelf buttressing is far from straightforward.

Several recent studies apply whole-Antarctic ice sheet models optimized to present-day observations towards improving our understanding for how Antarctic ice shelves limit flux across the grounding line (and by extension how they impact ice dynamics farther inland). Fürst and others (2016) calculated the buttressing across Antarctica ice shelves along two major directions (aligned with the ice flow and the second principle stress) and evaluated their impacts on upstream ice dynamics to identify regions of the ice shelves that are dynamically "passive"; in these regions increased submarine melting, or even complete removal of ice in these areas should not significantly alter local or regional ice dynamics or the flux of ice upstream. Reese and others (2018) used perturbation experiments to link small, localized decreases in ice shelf thickness to changes in integrated grounding line flux (GLF), thereby providing a map of GLF sensitivity to local increases in submarine melt rates. **Add some discussion here about the recent Goldberg et al. paper as well?**

Motivated by these studies, we build on and extend the methods and analysis of Fürst and others (2016) and Reese and others (2018) in order to make progress towards answering the following questions: (1) How do local and regional changes in ice shelf geometry affect distal changes in GLF? (2) Can local or regional ice shelf dynamics explain GLF sensitivity to local or regional changes in ice shelf thickness? (3) Can we derive and define new tools and analyses for understanding how observed or modeled spatial patterns in submarine melting influence GLF and, by extension, project how changes in submarine melt pattern and magnitude will impact GLF in the future?

Below, we first provide a brief description of the ice sheet model used in our study. We follow with a description of the model experiments and a discussion of the experimental results and their interpretation. We then demonstrate and discuss the pros and cons of a number of possible metrics for quantifying GLF sensitivity to changes in submarine melt. Based on limitations in all metrics explored here, we conclude by proposing and demonstrating an adjoint-based calculation that provides a sensitivity map analogous to that from the Reese and others (2018) perturbation experiments but at the cost of a single model adjoint solve. (**TZ: we should revisit this paragraph at some point after we finish most of revisions in the manuscript. SP: Agreed. It could be that some of the correlations you show w/ just the first principle stress are also worthy of highlighting as being reasonably good too.**)

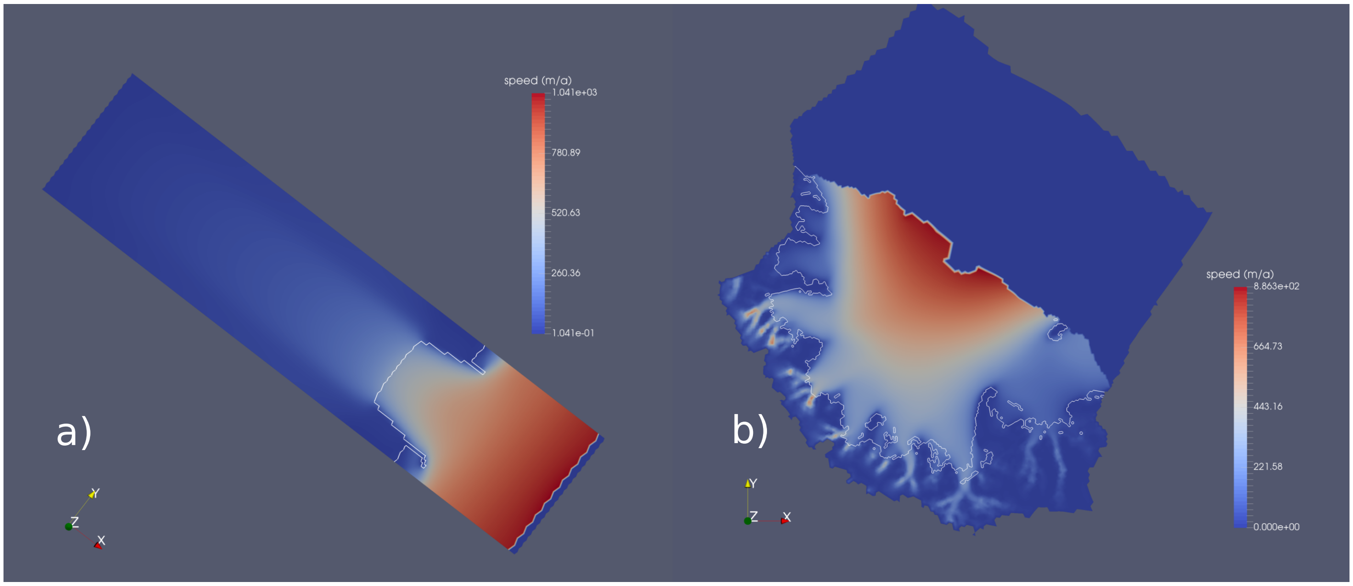

Fig. 1. Plan view of steady-state surface speed for MISMIP+ (a) and Larsen C ice shelf (b). The white curves show the grounding lines.

MODEL DESCRIPTION

SP: I built out this section a bit more. We can reduce later on if needed but it seemed a bit too thin. Note that this is mostly copied and lightly edited from the MALI paper, so we'll have to look over carefully and make sure it doesn't end up looking self-plagiarized. We use the MPAS-Albany Land Ice model (MALI; Hoffman and others (2018)), which solves the three-dimensional, first-order approximation to the Stokes momentum balance for ice flow[2]. Using the notation of Perego and others (2012) and Tezaur and others (2015a) this can be expressed as,

$$\begin{cases} -\nabla \cdot (2\mu_e \dot{\boldsymbol{\epsilon}}_1) + \rho_i g \frac{\partial s}{\partial x} &= 0, \\ -\nabla \cdot (2\mu_e \dot{\boldsymbol{\epsilon}}_2) + \rho_i g \frac{\partial s}{\partial y} &= 0, \end{cases} \tag{1}$$

where x and y are the horizontal coordinate vectors in a Cartesian reference frame, $s(x, y)$ is the ice surface elevation, ρ_i represents the ice density, g the acceleration due to gravity, and $\dot{\boldsymbol{\epsilon}}_{1,2}$ are the two dimensional strain rate vectors given by

$$\dot{\boldsymbol{\epsilon}}_1 = \begin{pmatrix} 2\dot{\epsilon}_{xx} + \dot{\epsilon}_{yy}, & \dot{\epsilon}_{xy}, & \dot{\epsilon}_{xz} \end{pmatrix}^T, \tag{2}$$

[2]See Schoof and Hewitt (2013) for for a full description of the Stokes momentum balance for ice flow and its lower-order approximations.

and

$$\dot{\boldsymbol{\epsilon}}_2 = \begin{pmatrix} \dot{\epsilon}_{xy}, & \dot{\epsilon}_{xx} + 2\dot{\epsilon}_{yy}, & \dot{\epsilon}_{yz} \end{pmatrix}^T. \tag{3}$$

The "effective" ice viscosity, μ_e in Equation 1, is given by

$$\mu_e = \gamma A^{-\frac{1}{n}} \dot{\epsilon}_e^{\frac{1-n}{n}}, \tag{4}$$

where γ is an ice stiffness factor, A is a temperature-dependent rate factor, $n = 3$ is the power-law exponent, and the effective strain rate, $\dot{\epsilon}_e$, is defined as

$$\dot{\epsilon}_e \equiv \left(\dot{\epsilon}_{xx}^2 + \dot{\epsilon}_{yy}^2 + \dot{\epsilon}_{xx}\dot{\epsilon}_{yy} + \dot{\epsilon}_{xy}^2 + \dot{\epsilon}_{xz}^2 + \dot{\epsilon}_{yz}^2\right)^{\frac{1}{2}}. \tag{5}$$

Gradients in the horizontal velocity components, u and v, contribute to the individual strain rate terms in Equation 5 and are given by

$$\dot{\epsilon}_{xx} = \frac{\partial u}{\partial x}, \quad \dot{\epsilon}_{yy} = \frac{\partial v}{\partial y}, \quad \dot{\epsilon}_{xy} = \frac{1}{2}\left(\frac{\partial u}{\partial y} + \frac{\partial v}{\partial x}\right), \quad \dot{\epsilon}_{xz} = \frac{1}{2}\frac{\partial u}{\partial z}, \text{ and } \dot{\epsilon}_{yz} = \frac{1}{2}\frac{\partial v}{\partial z}. \tag{6}$$

A stress free upper surface is enforced through

$$\dot{\boldsymbol{\epsilon}}_1 \cdot \mathbf{n} = \dot{\boldsymbol{\epsilon}}_2 \cdot \mathbf{n} = 0, \tag{7}$$

where $\mathbf{n}$ is the outward pointing normal vector at the ice sheet upper surface, $z = s(x, y)$. The lower surface is allowed to slide according to the continuity of basal tractions,

$$2\mu_e \dot{\boldsymbol{\epsilon}}_1 \cdot \mathbf{n} + \beta u = 0, \;\; 2\mu \dot{\boldsymbol{\epsilon}}_2 \cdot \mathbf{n} + \beta v = 0, \tag{8}$$

where β is a spatially variable, linear-friction coefficient. On lateral boundaries in contact with the ocean, the portion of the boundary above sea level is stress free while the portion below sea level feels the ocean hydrostatic pressure according to

$$2\mu_e \left(\dot{\boldsymbol{\epsilon}}_1 \cdot \mathbf{n}, \, \dot{\boldsymbol{\epsilon}}_2 \cdot \mathbf{n}, \, 0\right)^T - \rho_i g(s - z)\mathbf{n} = \rho_o g \max(z, 0)\mathbf{n}, \tag{9}$$

where ρ_o represents the density of ocean water and $\mathbf{n}$ the outward pointing normal vector to the lateral boundary (i.e., parallel to the (x, y) plane).

A more complete description of the full MALI model, including the implementations for mass and energy conservation, can be found in Hoffman and others (2018). Additional details about the Albany momentum balance solver can be found in Tezaur and others (2015a,b).

Here, we apply MALI to experiments on both idealized and realistic marine-ice sheet geometries. For our idealized domain and model state, we start from the equilibrium initial conditions for the MISMIP+ experiments, as described in Asay-Davis and others (2016) and Cornford and others (MISMIP+ papers) (**TZ: is it the same paper as Xylar's? SP: No, I meant the actual MISMIP+ results paper, which Steph C. is supposed to be writing.**). The model mesh is spatially uniform at 2 km resolution. For our realistic domain, we use Antarctica's Larsen C ice shelf and its upstream catchement area. The model state is based on the optimization of the ice stiffness (γ in Equation 4) and basal friction (β in Equation 8) coefficients in order to provide a best match between modeled and observed present-day velocities (Rignot and others, 2014) using adjoint-based methods discussed in Perego and others (2014) and Hoffman and others (2018). The domain geometry is based on BEDMAP2 (Fretwell and others, 2013) and ice temperatures, which are held fixed for this study, are based on Liefferinge and Pattyn (2013). Mesh resolution on the ice shelf is between 2 and 6 km and coarsens to 20 km in the ice sheet interior. Following optimization to present-day velocities, the model is relaxed using a 100 year forward run, providing the initial condition from which the Larsen C experiments (discussed below) are conducted. Both the MISMIP+ and Larsen C experiments use 10 vertical layers that are finest near the bed and coarsen towards the surface (4% and 23% of the total thickness, respectively). The grounding line position is determined from hydrostatic equilibrium. A sub-element parameterization, analogous to method SEP3 from Seroussi and others (2014), is used to define basal friction coefficient values at the grounding line.

PERTURBATION EXPERIMENTS

To explore the sensitivity of changes in GLF to small changes in ice shelf thickness, we conduct a number of perturbation experiments analagous to those of Reese and others (2018). Using diagnostic model solutions, we first study the instantaneous response of GLF for the idealized geometry and initial state provided by the MISMIP+ experiment (Asay-Davis and others, 2016). We then conduct a similar study for Antarctica's Larsen C ice shelf but using a realistic configuration and initial state.

Our experiments are conducted in a manner similar to those of Reese and others (2018). We perturb the coupled ice sheet-shelf system by decreasing the ice thickness uniformly by 1 m over square grid "boxes" covering the base of the ice shelves, after which we examine the instantaneous impact on kinematics and dynamics (discussed further below). For MISMIP+, the uniform, 2 km mesh implies that grid cell centers naturally align with these boxes. For the Larsen C ice shelf, horizontal mesh resolution is spatially variable and we assign each grid cell to fall within one and only one box based on its location. For MISMIP+, we use 2×2 km square boxes that coincide with the actual grid cell size. For Larsen C, we only use 20×20 km square boxes (i.e., as in Reese and others (2018)). Lastly, for the MISMIP+ 2 km experiments we note that, in order to save on computing costs, we only perturb the region of the ice shelf for which $x < 530$ km (the area over which the ice shelf is likely lateraly buttressed) and $y > 40$ km (one half of the ice shelf due to the symmetry about the centerline). While we only perturb the ice shelf over one half of the centerline, we analyze the response to those perturbations over the entire model domain.

Similar to Reese and others (2018), we define a GLF "response number",

$$N_r = \left(\frac{R}{P}\right)^k, \tag{10}$$

where R is the ice flux change integrated along the entire grounding line, P is the mass associated with a single grid box perturbation (e.g., 2 km×2 km ×0.001 km for the MISMIP+ perturbation experiments) and k is a power-law index that allows for the possiblity of a nonlinear relationship between ice shelf buttressing and the change in GLF (see also Schoof (2007)). Here, we use $k = 1/n$ with $n = 3$.

Despite the existence of many possible factors linking GLF to ice shelf properties (ice flow direction, horizontal gradients in ice shelf geometry, stress fields, strain-rate fields, perturbation locations, etc.), here we mainly examine model stress fields and the distance between perturbations and the GL. This is because, as we show below, these factors correlate closely with the sensitivity of changes in GLF to the imposed ice shelf perturbations. To incorporate the local stress field and its buttressing capacity into our analysis, we also calculate a "buttressing number", (N_b), analagous to that from Fürst and others (2016) (Eqn 11),

$$N_b = 1 - \frac{\sigma_{nn}}{N_0}, \tag{11}$$

where N_0 is the vertically integrated ocean pressure ($N_0 = 0.5\,(1 - \rho_i/\rho_w)\,gH$) and ρ_i (910 kg m^3) and ρ_w (1028 kg m^3) are the density of ice and ocean water, respectively. σ_{nn} is the normal stress along a specific horizontal direction, which we discuss further below.

RESULTS AND DISCUSSIONS

Correlation between the buttressing number and changes in GLF

A decrease in ice shelf buttressing tends to lead to an increase in GLF (e.g., Gagliardini and others, 2010) and intuitively we expect that the GLF should be relatively more sensitive to melt changes that occur in regions of relatively larger buttressing. Here, we aim to better understand and quantitfy the relationship between the buttressing "strength" (given by N_r) and corresponding changes in GLF (given by N_r). Can we quantify the predicted change in GLF for a given buttressing number (N_b) and melt perturbation? In Figure 2, we show correlations between N_b and N_r for perturbations applied to the MISMIP+ domain when N_b from Equation 11 sets σ_{nn}=σ_{p1}, with σ_{p1} being the first principle stress[3]. In Figure 2b, we include all perturbed ice shelf locations in the comparison and find relatively week N_b-N_r correlations. In Figure 2c, we remove from the comparison points that are 1) weakly buttressed ($x > 480$, where the ice shelf becomes unconfined) and 2) within 5 km of the GL, and a much stronger N_b-N_r correlation emerges. In Figure 2d, we plot the N_b-N_r correlation for locations where $x > 480$ and the magnitude of the thickness gradient is $< 7\text{x}10^{-3}$. The strong similarities between Figures 2c and 2d suggest that the seemingly *ad hoc* "distance from the grounding line" constraint is important for removing areas of complex geometry (and hence complex dynamics) from the N_b-N_r comparisons.

Correlation dependence on buttressing direction

According to Equation 11, the buttressing number N_b is computed using the normal stress (σ_{nn}) along a specified direction. Therefore, the buttressing number at any perturbation point can vary depending on the chosen direction. Fürst and others (2016) calculated N_b along two directions, the ice flow direction and the direction corresponding to the second principle stress (σ_{p2}), and found that the latter – the direction corresponding to the maximum compressive stress (or the least extensional stress) – has the maximum impact on the "passive" ice shelf regions. In Figure 3, we plot the correlation coefficients (r^2) between N_r and N_b using values for σ_{nn} that vary continuously by an angle $\Delta\phi$, between 0 and 180 degrees, relative to the direction of σ_{p1}. We find the largest correlation coefficient ($r^2 > 0.9$) when N_b is aligned with the σ_{p1} direction ($\Delta\phi = 0°$) and the smallest correlation coefficient ($r^2 < 0.4$) when N_b is aligned with the σ_{p2} direction ($\Delta\phi = 90°$).

This can be further testified by looking at the angle differences between σ_{p1} and flow directions ($\Delta\phi = \phi_{flow} - \phi_{\sigma_{p1}}$). From Figure 3b, we see that for around 50% of the perturbation points, their flow directions are around 30–50 degree more than the σ_{p1} directions, which is consistent with the phase differences in Figure 3a. If we add around 40 degree on top of the flow direction (blue curve), the new direction will be likely aligned closely with the σ_{p2} direction, which is consequently pointing to the smallest r^2 number for the σ_{p1} (red) curve. This indicates that the local maximum buttressing relating to σ_{p2} is unnecessarily corresponding to the integrated instantaneous GLF responses. (**SP: I tried to reword this**

[3] We expand on our reasons for choosing σ_{p1} below.

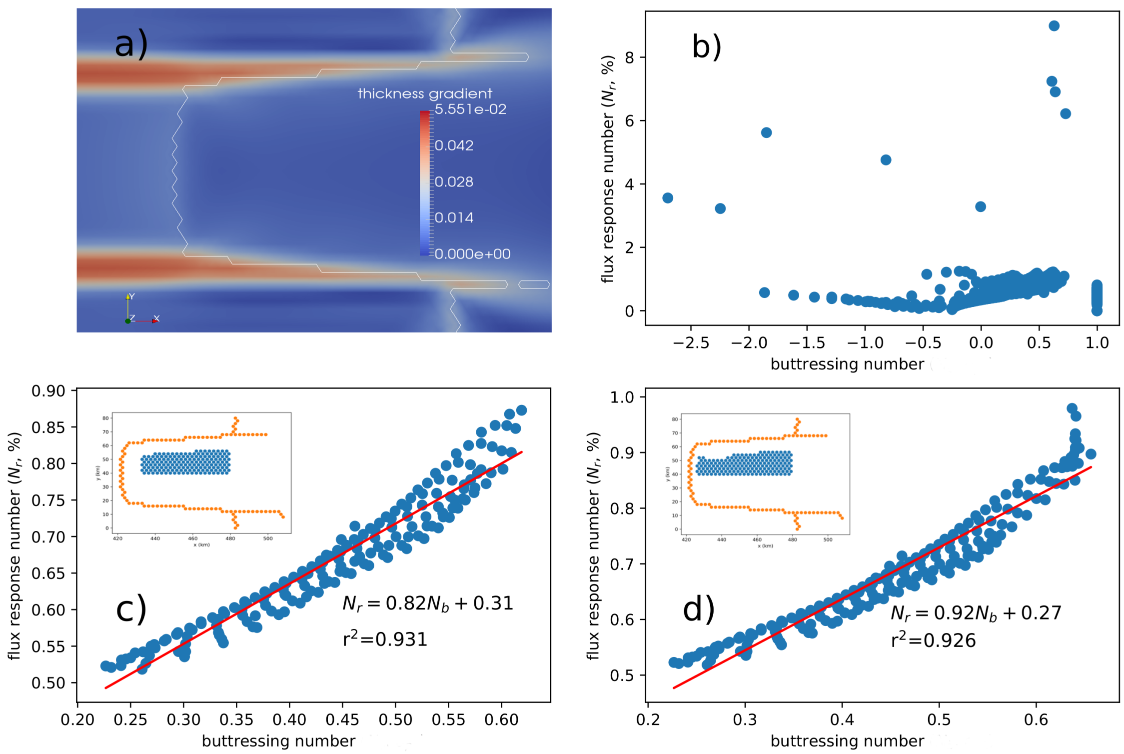

Fig. 2. (a)MISMIP+ steady-state geometry. Color represents the magnitude of the ice thickness gradient and the white line represents the GL. (b) N_b-N_r correlation for all perturbation points. (c) N_b-N_r correlation for perturbation points satisfying $x > 480$ and that are >10 km away from GL; (d) N_b-N_r correlation for perturbation points satisfying $x > 480$ and with a thickness gradient magnitude of $< 7\text{x}10^{-3}$. In (c) and (d), the red (blue) dots in the insets represent the GL (perturbation) grid cells.

so that it is a bit more clear, but I failed (commented out my new version of it). I'm going to leave it for the time being and come back to it later. But I also wonder if this discussion is necessary or if it is just too confusing.)

Understanding the dependence on buttressing direction

The strong correlation between changes in GLF and the first principle stress can be understood by examining the spatial patterns of velocity change[4] and stress change associated with thickness perturbations. In Figure 4, we plot histograms of the maximum (red) and minimum (blue) velocity changes as a function of angular distance (??) around each perturbation point for the case where σ_{nn} is calculated

[4]In this case, velocity changes are a proxy for flux changes since ice thickness is changed only at the perturbation level.

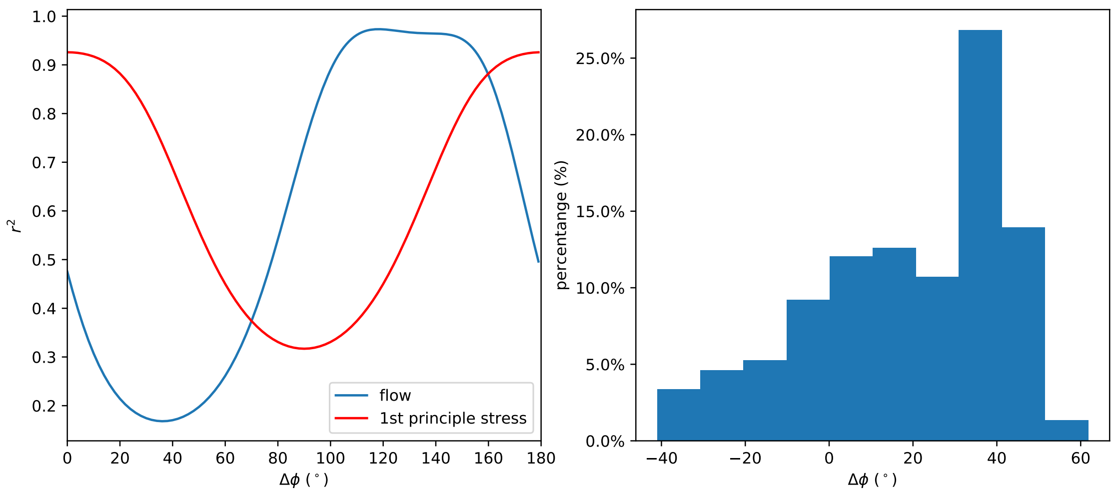

Fig. 3. (a) N_b-N_r correlation coefficients for σ_{nn} values rotated anti-clockwise by $\Delta\phi$ degrees relative to the σ_{p1} direction (red)and the ice flow direction (blue). (b) Histogram of the angular differences between the flow direction and σ_{p1} directions. The perturbation points analyzed here are those shown in Figure 2d.

along the ice flow direction or along the σ_{p1} direction. Figures 4a and b include all perturbation points while Figures 4c and d contain only the points from Figure 2d (i.e., filtered according to ice thickness gradient). For σ_{nn} calculated along the ice flow direction (Fig 4a,b), the maximum velocity changes cluster around the flow direction, while the minimum velocity changes cluster around 120 degrees to the flow direction. For σ_{nn} calcualted along the σ_{p1} direction (Fig 4c,d), the maximum velocity changes cluster between 0 and 45 degrees of the σ_{p1} direction and the minimum velocity changes cluster between 90 and 120 degrees. From this analysis, it is clear that most of the maximum (minimum) velocity changes are aligned with the first (second) principle stress direction, supporting the hypothesis that the first principle stress direction is more important for ... *not sure how to close this yet. Something about how changes propagate more easily along p1 even though p2 "controls" the buttressing? Not sure we entirely understand this yet but we need to.*

Further evidence for the importance of the first principle stress direction is given by the variances that characterize the changes in the state of stress and the state of velocity between the initial condition and the perturbation experiments. To this end, we define the metric Ψ,

$$\Psi = \frac{\sigma_p - \sigma_c}{\sigma_c} - \frac{u_p - u_c}{u_c}, \tag{12}$$

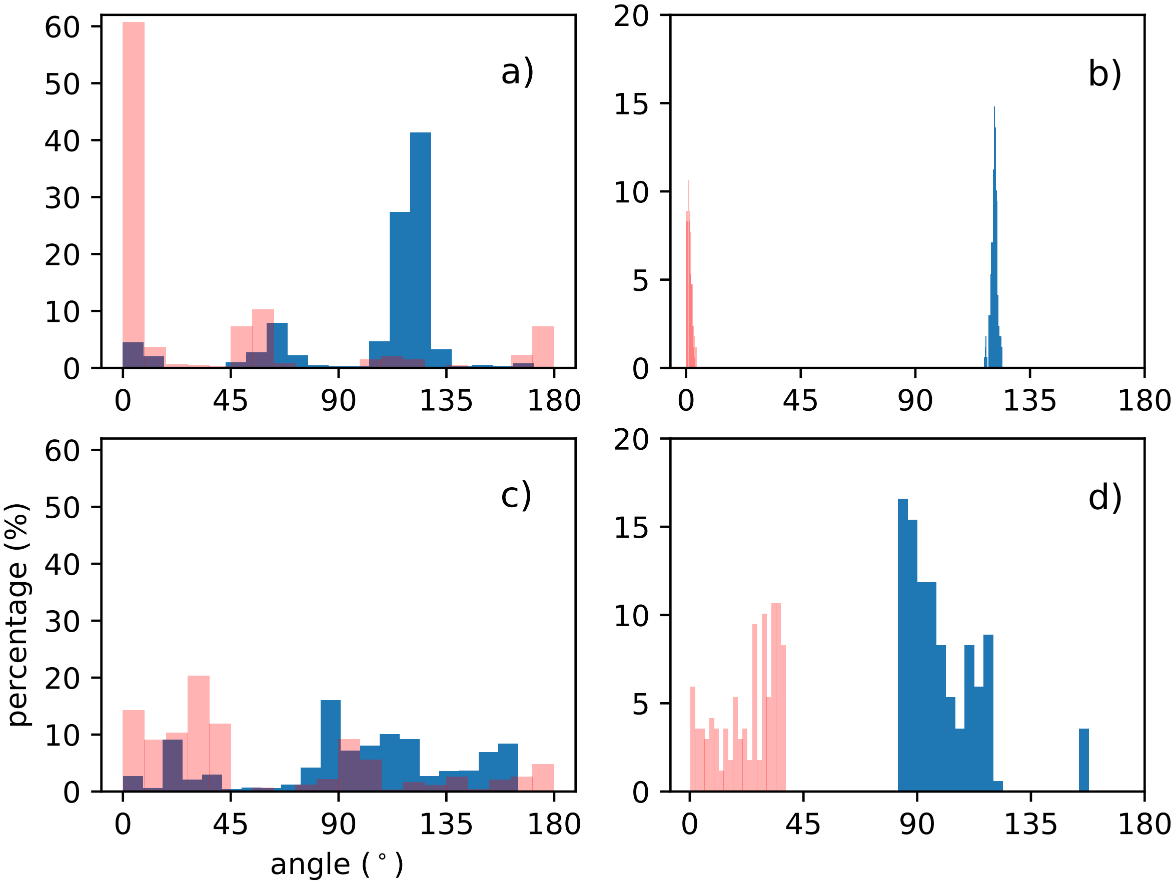

Fig. 4. Histograms for the frequency of the maximum (red) and minimum (blue) velocity changes in neighboring grid cells as a function of angular distance around each perturbation point. In a and c, all perturbation points are shown and in plots b and d, only the subset of points from Figure 2d (b and d) are shown. (**TZ: this figure still needs double check!**)

where the subscripts p and c denote the perturbation experiments and the "control" (i.e., the initial condition), respectively, and σ and u denote the stress component and ice velocity, respectively. This metric is a measure of the consistency between changes in the model stress and velocity states between the control (the initial condition) and perturbation experiments. We calculate Ψ at every grid point for the case where σ_{nn} in Equation 11 is set equal to σ_{p1} (Fig 5a) and σ_{p2} (Fig 5b). From Figure 5, it is clear that the variance between stress and velocity change is much smaller everywhere in the domain, including along the GL, for the case of $\sigma_{nn} = \sigma_{p1}$. Physically this can be interpreted as demonstrating a stronger correlation between changes in the first principle stress component and the velocity (or flux) than between changes in the second principle stress. *SP: Or something like this. Need to think about it some more still. I wonder*

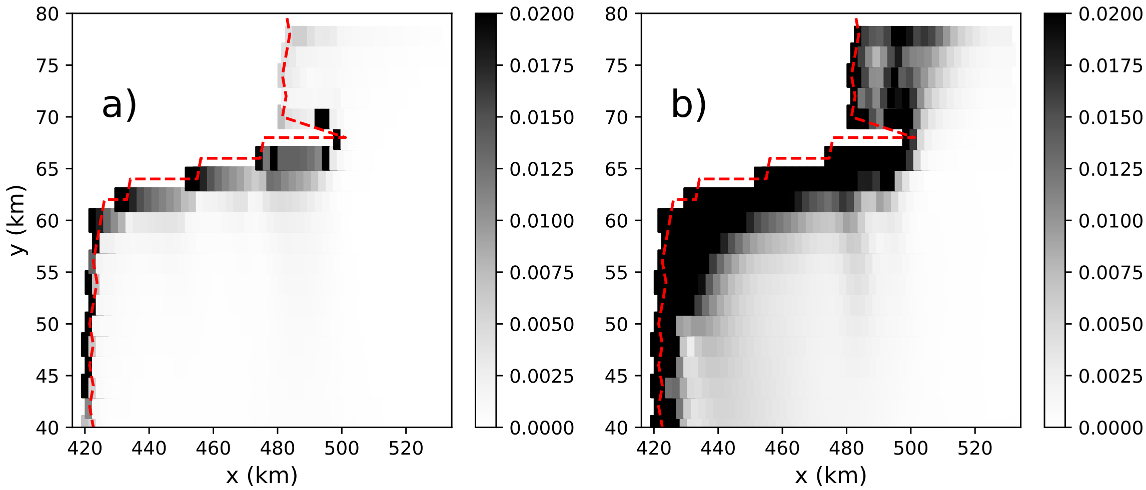

Fig. 5. The standard deviations of Ψ – a metric for how closely a change in normal stress corresponds with a change in velocity – at each perturbation point of the MISMIP+ domain, for the case of $\sigma_{nn} = \sigma_{p1}$ (a) and $\sigma_{nn} = \sigma_{p2}$ (b).

if it could also be interpreted differently – e.g., in 5b, could the much larger variance be because a small change in p2 results in a much larger change in velocity (relative to p1)?. Would it make more sense for Fig. 5 to be an actual correlation coeff. plot rather than the somewhat complicated variance comparison?. Examination of the stress and velocity changes at the GL for a perturbation at a specific location on the ice shelf provides further evidence of a strong (weak) correlation between changes in the first principle stress (second principle stress) and changes in the velocity (Figure 6).

SP: Leaving this section alone for now. I think it's worth including some additional discussion here if we can make some reasonable speculation as to what's going on. But we probably need to come up with a bit more than this. I wonder if there are other T3 folks who might have some insight into this problem? One thing that occurs to me is that we could be conflating cause and effect here. For example, when we look at Figure 6, it looks like the changes in velocity correlate with changes in σ_{p1}, whereas they don't correlate with changes in σ_{p2}. But it could simply be that the changes in σ_{p2} (due to the thickness perturbation) are causing a velocity change, and the velocity change is better reflected by the change in σ_{p1}. This makes sense at the GL, where we know the velocity / flux are largely going to be aligned with the σ_{p1} direction (perpendicular to the GL). This doesn't, however, explain why we see a good correlation between changes in velocity / flux at the GL (reflected by the flux response number, N) and σ_{p1} but a much poorer correlation between the flux response number and σ_{p2}. One of the possible reasons for us seeing such direction-dependent correlations might be due to the perturbation propagation features on ice shelves. The energy of perturbation propagates

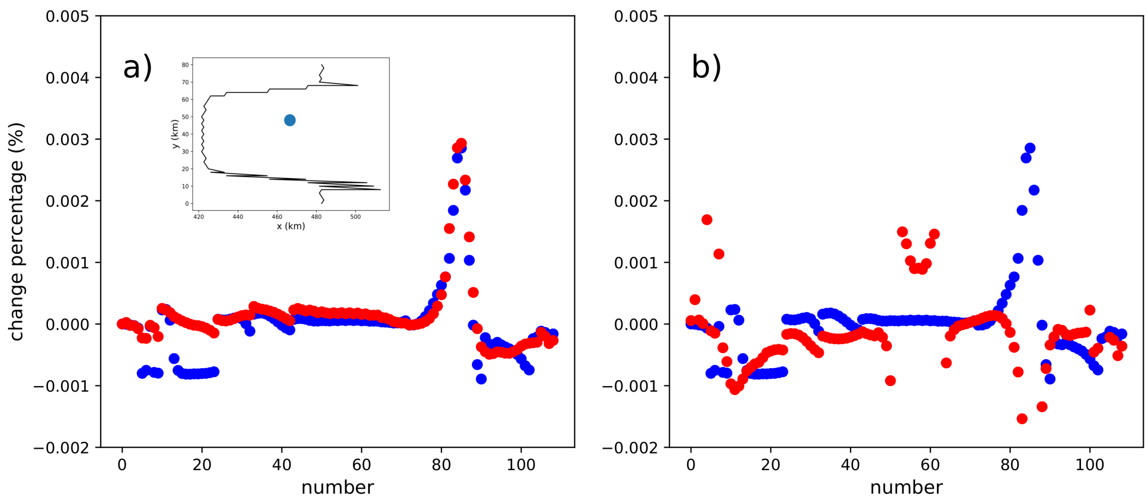

Fig. 6. Relationship between GL changes in the velocity (blue) and in the stress (red) for the MISMIP+ test case due to a perturbation at a specific location on the ice shelf (blue dot in inset map). In a), changes in GL velocity are plotted against changes in σ_{p1} and in b) changes in GL velocity are plotted against changes in σ_{p2}. The x-axis is an index for the grid cell number along the GL.

with the group velocity if we decompose it using Fourier transform. A similar example can be found in (Gudmundsson, 2003). Using very simplified geometry Gudmundsson (2003) analyzed the propagation of basal perturbation to glacier surface and found that the direction of group velocity is aligned closely with the main flow. The existence of preferred propagation direction for the perturbations can possibly lead to our findings that favor the first principle stresses (**TZ: I am still not able to explain why it's exactly the first principle stress direction :(**).

Application to Larsen C ice shelf

To explore whether the correlations between N_b-N_r for the MISMIP+ test case hold for realistic ice shelves, we apply a similar analysis to our Larsen C domain. In this case, the computational mesh resolution varies, from finer near the GL (xx km) to coarser towards the center of the ice shelf and calving front (yy km). We use 20 km $\times$ 20 km boxes for the application of ice thickness perturbations (as in Reese and others (2018)) where the number of grid cells contained within each perturbation "box" is adjusted in order to sum to the correct area. Additionally, to account for the complex geometry of the Larsen C ice shelf (i.e., the GL shape, the existence of ice rises, etc.), we apply two different sets of perturbation experiments, both with and without perturbations applied to boxes containing the GL.

Analagous to Figures 3a,b for the MISMIP+ test case, Figures 7a,b shows the correlations between N_b and N_r for the Larsen C model domain. As previously, calculating N_b using $\sigma_{nn} = \sigma_{p1}$ provides the best overall correlation between N_b and N_r (red curve for $\Delta\phi = 0°$) and calculating N_b using $\sigma_{nn} = \sigma_{p2}$ provides the worst overall correlation (red curve for $\Delta\phi = 90°$). **SP: As noted above, I'm not sure about introducing the discussion about results relative to the velocity direction, as I think they are maybe just confusing. So leaving this next part alone for now.** The phase difference between the σ_{p1} and flow direction results can also be partially explained by their respective angle differences. In Figure 7b we can find the angles of flow directions are mostly around 90–100 degrees larger than that of the σ_{p1} directions. This is a bit biased than the around 70 degree difference in Figure 7a. However, considering the stress values (and thus N_b) for each perturbation box are averaged over multiple cells, we argue this difference is probably an acceptable error during our calculation.

In Figures 7c, d we include points near to the GL in the analysis, which 1) reduces the r^2 values and 2) changes the relationship between the correlation coefficients and the direction aligned with σ_{p1}. Specifically, while the direction aligned with σ_{p2} still gives the worst correlation between N_b and N_r, the direction giving the best correlation is rotated by approximately 40° relative the direction associated with σ_{p1}. *SP: I'm not really sure what else we can say about this, other than that it's an indication that using σ_{p1} and σ_{p2} in the calculation of N_b is probably just more problematic for complex geometries.*

Impacts of near-GL perturbations

For the near-GL perturbations, it is hard to find similar linear regression relationship as discussed above. Alternatively, they are largely controlled by the distance between GL and perturbation points and also by the geometric features around them. As the perturbation decays over distance (Lick, 1970), the neighboring GL cells of those near-GL perturbations will relatively easily detect the perturbation energy. This can be verified by looking at the standard deviations of GL velocity change due to each perturbation (Fig 8). For perturbations close to GL, their corresponding GL flux changes are in general confined to local regions, while in the remote GL sections the velocity changes are often negligible, resulting in large standard deviations. This can possibly cause spatial heterogeneity of GL retreating if the sub-shelf melting is very close to GL and is heavily local confined.

The propagation of perturbation can also be impacted by the spatial GL geometry, e.g., they can be blocked by the local GL. For example, the perturbation at around x = 480 km and y = 65 km in Figure 8a can not directly impact the ice flow on the other side of the grounded peninsula (e.g., x=485 km, y=70km)

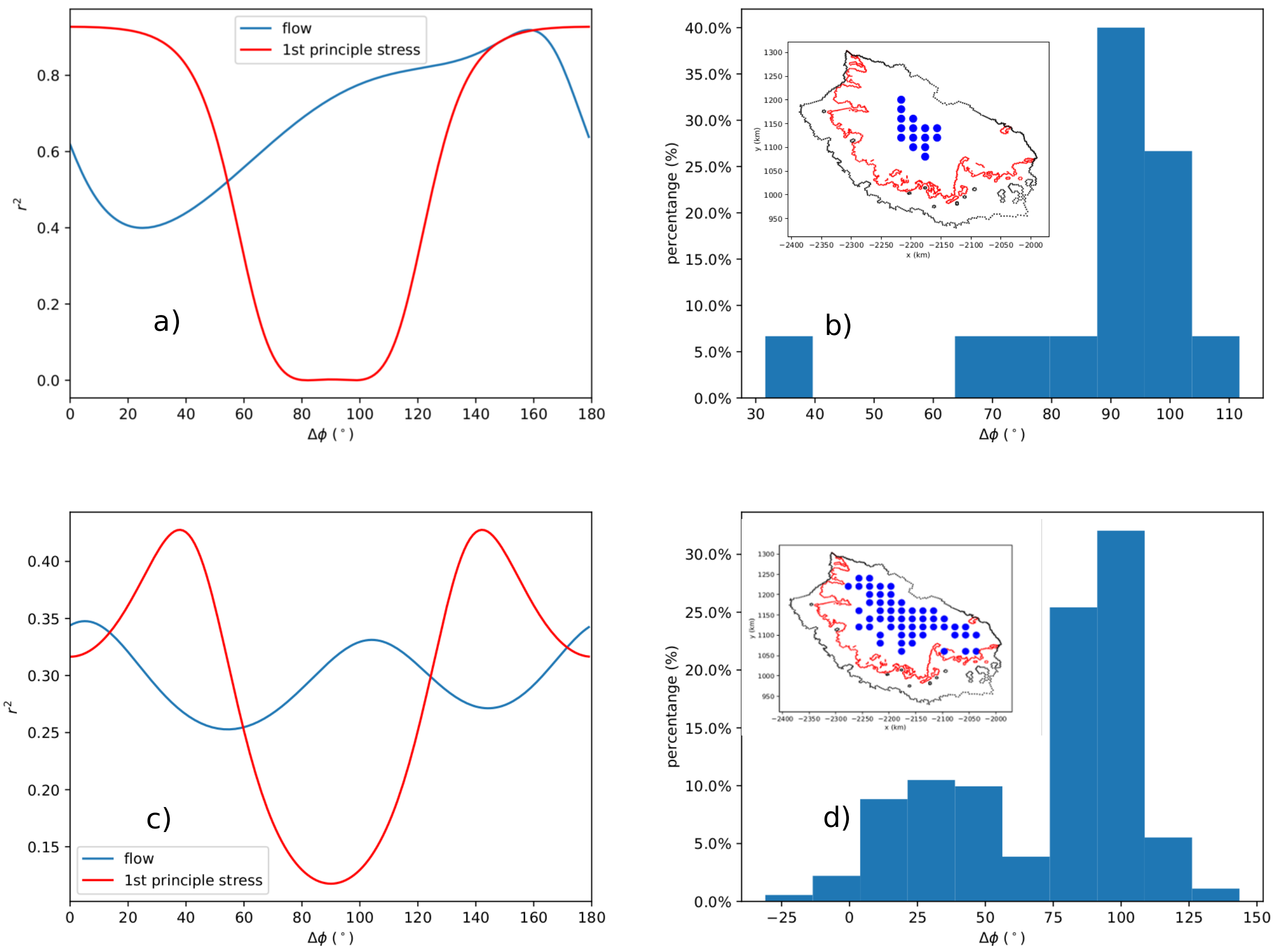

Fig. 7. (a, c) The N_b-N_r regression coefficients for each direction rotated anti-clock-wisely from the σ_{p1} (red) and flow direction (blue); (b, d) The histogram of the angle differences between flow and σ_{p1} directions. The insets in b) and d) show the perturbation boxes (blue circles).

in the same way as for it's neighboring cells. This is one of the major factors that complicate our diagnostic analysis for real ice shelves (for example, Larsen C) containing complex GL shapes and geometries. *SP: Is there any way we could show this? E.g., for the Larsen C test case, could we plot the local GLF changes for a perturbation that is partly hidden behind an island / penn? We might actually be able to see the "shadowing" in the case. That is, we might be able to see that the portion of the GL that is blocked from a perturbation has a GLF that doesn't change much whereas nearby points along the GL that aren't block do change. I think this would just require plotting some maps from individual perturbation experiments for locations around some of these types of features.*

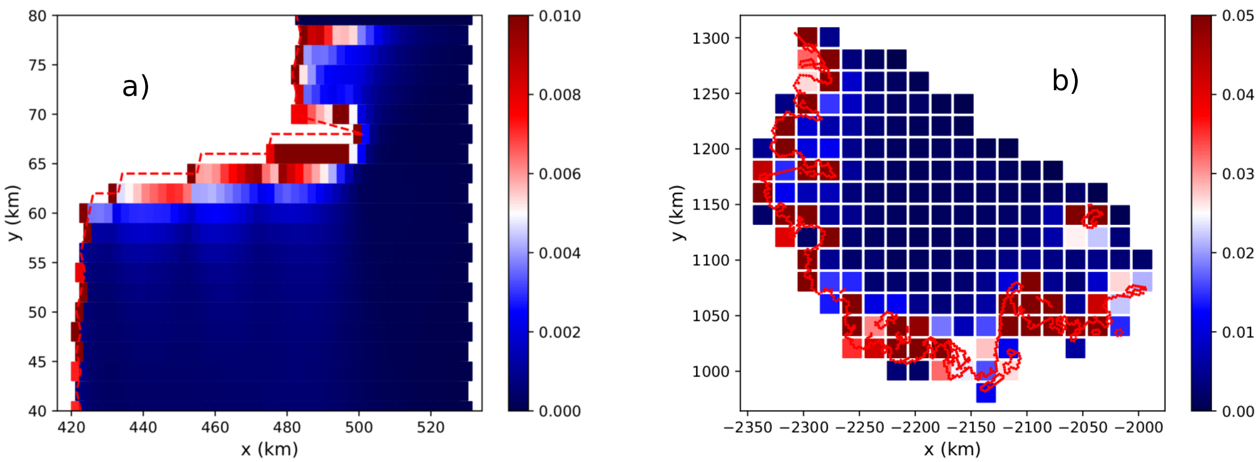

Fig. 8. Standard deviation of velocity change along GL for each perturbation point for the MISMIP+ (a) and Larsen C (b) experiment. The red dashed lines (points) are the GLs for MISMIP+ (a) and Larsen C (b) .

Adjoint sensitivity

Another altogether different approach to diagnosing the sensitivity of the flux across the grounding line to changes in ice shelf geometry is provided by the adjoint approach. This approach provides results analogous to those presented and discussed above but at a greatly reduced cost (and with improved accuracy?): rather than using the forward model to examine the sensitivity of GLF change to perturbations at each of n model grid cells, a single adjoint solve is used to deduce those same sensitivities *simultaneously* at all n grid cells.

SP: Will need Mauro to fill in some of the technical details here.

In Figure 9, we provide a demonstration for the case of the MISMIP+ domain by comparing sensitivities deduced from X individual forward model evaluations (i.e., the perturbation experiments discussed above, and analagous to those in Reese and others (2018)) with those deduced from a single model adjoint solve. Here, the "sensitivity" is defined as BLAH. *SP: need more information on techincal deatils here.*

The comparison in Figure 9 demonstrates that, for points in the domain we expect to be comparable, the two approaches provide a near exact match. While we cannot provide definitive proof, we suggest that the disagreement in sensitivity near the GL is likely a result of errors in the forward modeling approach, which prohibit us from controlling errors associated with the choice of a finite perturbation size (other reasons?).

CONCLUSIONS

From this study we find that the sensitivity of grounding line (GL) flux to melt perturbations beneath ice shelves appears to be linearly related to the buttressing number for certain stress field of the ice flow

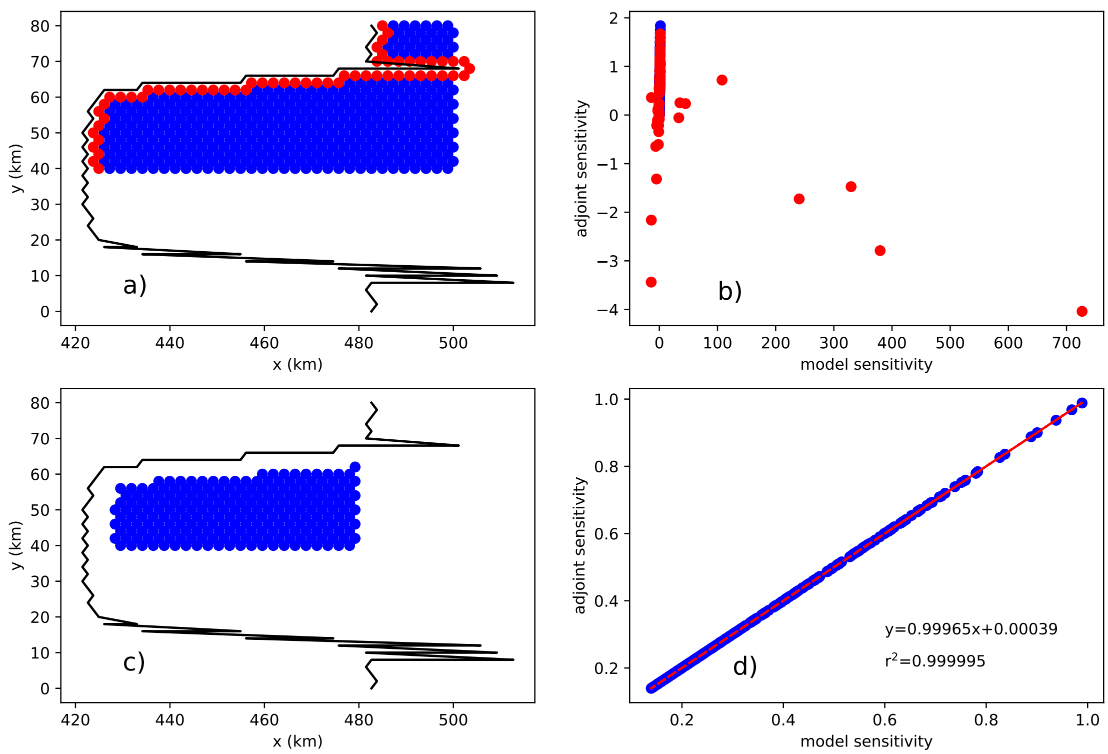

Fig. 9. Grounding line flux sensitivity for the MISMIP+ domain calculated from individual perturbation experiments versus derived from a model adjoint (perturbation locations are shown by circles in a and c). Perturbation-experiment (x-axis) and adjoint-derived (y-axis) sensitivities (see text for definition) are plotted against one another in b and d. In a and b, the red circles indicate near-GL (<2 km) perturbation points, which are omitted in the comparison in b and d. The GL in a and c is shown by the black curve. In b and d, the red line is a linear regression between the perturbation-experiment and adjoint-derived sensitivities.

regime when the perturbations are located near the center of ice shelves. We can divide an ice shelf into three different geometric regions: 1) near GL where the shear margins dominate; 2) near the calving fronts where ice can be considered as "passive" and 3) the central regions of ice shelf. Though it is ambiguous to indentify the boundaries of those three sub-regions, we find that both the shear margins and passive ice regions show very weak linear connections to GL flux changes. The shear margins are strongly impacted by the upstream grounded stream flows and the passive ice shelf basically has negligible contribution to GL dynamics.

The buttressing of ice shelf resists ice flows from upstream. The maximum buttressing number (calculated from the second principle stress σ_{p2}) is a commonly used metric to quantify the buttressing effects of ice shelf, doesn't show clear correlations to the changes of GL flux. Among many possible factors we find that the distance away from perturbation locations may be a critical control for perturbation propagation across ice shelves, which is important for understanding the relationships between the stress field of the ice shelf and the GL flux changes. The GL ice speed changes may be more correlated to the changes of the first principle stress (σ_{p1}) and normal stress along flow (σ_f) than other stress components, for example, the second principle stress (σ_{p2}) and the shear stress (σ_s), indicating that the stress component (σ_{p2}) that contribute significantly to buttressing is not necessarily related to the progapation of buttressing.

The linear N_b-N_r relationships presented in this study are based on small (1 m) thickness perturbations. However, it's still unclear if they can stand for large melts at the bottom of ice shelves (**Perhaps we also need to do large perturbation experiments?**). Despite the progress we have made in this study, we suggest to apply a fully-developed perturbation propagation model for further understanding the physics of GL flux changes under ocean forcings.

ACKNOWLEDGEMENT

REFERENCES

Asay-Davis XS, Cornford SL, Durand G, Galton-Fenzi BK, Gladstone RM, Gudmundsson H, Hattermann T, Holland DM, Holland D, Holland PR and others (2016) Experimental design for three interrelated marine ice sheet and ocean model intercomparison projects: Mismip v. 3 (mismip+), isomip v. 2 (isomip+) and misomip v. 1 (misomip1). *Geoscientific Model Development*, **9**(7), 2471–2497

Barletta VR, Bevis M, Smith BE, Wilson T, Brown A, Bordoni A, Willis M, Khan SA, Rovira-Navarro M, Dalziel I and others (2018) Observed rapid bedrock uplift in amundsen sea embayment promotes ice-sheet stability. *Science*, **360**(6395), 1335–1339

De Rydt J, Gudmundsson G, Rott H and Bamber J (2015) Modeling the instantaneous response of glaciers after the collapse of the larsen b ice shelf. *Geophysical Research Letters*, **42**(13), 5355–5363

Fretwell P, Pritchard HD, Vaughan DG, Bamber J, Barrand N, Bell R, Bianchi C, Bingham R, Blankenship D, Casassa G and others (2013) Bedmap2: improved ice bed, surface and thickness datasets for antarctica

Fürst JJ, Durand G, Gillet-Chaulet F, Tavard L, Rankl M, Braun M and Gagliardini O (2016) The safety band of antarctic ice shelves. *Nature Climate Change*, **6**(5), 479

Gagliardini O, Durand G, Zwinger T, Hindmarsh R and Le Meur E (2010) Coupling of ice-shelf melting and buttressing is a key process in ice-sheets dynamics. *Geophysical Research Letters*, **37**(14)

Gudmundsson G (2013) Ice-shelf buttressing and the stability of marine ice sheets. *The Cryosphere*, **7**(2), 647–655

Gudmundsson GH (2003) Transmission of basal variability to a glacier surface. *Journal of Geophysical Research: Solid Earth*, **108**(B5)

Gudmundsson H, Krug J, Durand G, Favier L and Gagliardini O (2012) The stability of grounding lines on retrograde slopes. *The Cryosphere*, **6**(6), 1497–1505

Hoffman MJ, Perego M, Price SF, Lipscomb WH, Zhang T, Jacobsen D, Tezaur I, Salinger AG, Tuminaro R and Bertagna L (2018) Mpas-albany land ice (mali): a variable-resolution ice sheet model for earth system modeling using voronoi grids. *Geoscientific Model Development*, **11**(9), 3747–3780 (doi: 10.5194/gmd-11-3747-2018)

Joughin I, Smith BE and Medley B (2014) Marine ice sheet collapse potentially under way for the thwaites glacier basin, west antarctica. *Science*, **344**(6185), 735–738

Lick W (1970) The propagation of disturbances on glaciers. *Journal of Geophysical Research*, **75**(12), 2189–2197

Liefferinge BV and Pattyn F (2013) Using ice-flow models to evaluate potential sites of million year-old ice in antarctica. *Climate of the Past*, **9**(5), 2335–2345

Mercer JH (1978) West antarctic ice sheet and co2 greenhouse effect: a threat of disaster. *Nature*, **271**(5643), 321

Morland L (1987) Unconfined ice-shelf flow. In *Dynamics of the West Antarctic Ice Sheet*, 99–116, Springer

Mutter K (1983) *Theoretical glaciology*

Pegler SS and Worster MG (2012) Dynamics of a viscous layer flowing radially over an inviscid ocean. *Journal of Fluid Mechanics*, **696**, 152–174

Perego M, Gunzburger M and Burkardt J (2012) Parallel finite-element implementation for higher-order ice-sheet models. *Journal of Glaciology*, **58**(207), 76–88, ISSN 00221430 (doi: 10.3189/2012JoG11J063)

Perego M, Price S and Stadler G (2014) Optimal initial conditions for coupling ice sheet models to earth system models. *Journal of Geophysical Research: Earth Surface*, **119**(9), 1894–1917

Reese R, Gudmundsson GH, Levermann A and Winkelmann R (2018) The far reach of ice-shelf thinning in antarctica. *Nature Climate Change*, **8**(1), 53

Rignot E, Mouginot J, Morlighem M, Seroussi H and Scheuchl B (2014) Widespread, rapid grounding line retreat of pine island, thwaites, smith, and kohler glaciers, west antarctica, from 1992 to 2011. *Geophysical Research Letters*, **41**(10), 3502–3509

Royston S and Gudmundsson GH (2016) Changes in ice-shelf buttressing following the collapse of larsen a ice shelf, antarctica, and the resulting impact on tributaries. *Journal of Glaciology*, **62**(235), 905–911

Schoof C (2007) Ice sheet grounding line dynamics: Steady states, stability, and hysteresis. *Journal of Geophysical Research: Earth Surface*, **112**(F3)

Schoof C (2012) Marine ice sheet stability. *Journal of Fluid Mechanics*, **698**, 62–72

Schoof C and Hewitt I (2013) Ice-sheet dynamics. *Annual Review of Fluid Mechanics*, **45**, 217–239

Seroussi H, Morlighem M, Larour E, Rignot E and Khazendar A (2014) Hydrostatic grounding line parameterization in ice sheet models. *The Cryosphere*, **8**(6), 2075–2087

Tezaur IK, Perego M, Salinger AG, Tuminaro RS and Price S (2015a) Albany/FELIX: a parallel, scalable and robust, finite element, first-order Stokes approximation ice sheet solver built for advanced analysis. *Geoscientific Model Development*, **8**, 1–24, ISSN 19919603 (doi: 10.5194/gmd-8-1-2015)

Tezaur IK, Tuminaro RS, Perego M, Salinger AG and Price SF (2015b) On the Scalability of the Albany/FELIX first-order Stokes Approximation ice Sheet Solver for Large-Scale Simulations of the Greenland and Antarctic ice Sheets. *Procedia Computer Science*, **51**, 2026–2035, ISSN 18770509 (doi: 10.1016/j.procs.2015.05.467)

Wearing M (2016) *The Flow Dynamics and Buttressing of Ice Shelves*. Ph.D. thesis, University of Cambridge

APPENDIX